Faraday Discussions

Cite this: DOI: 10.1039/d5fd00082c

PAPER

Exploration of nanostructured high-entropy alloys for key electrochemical reactions: a comparative study for the solid solution systems Cu–Pd–Pt–Ru, Ir–Pd–Pt–Ru and Ni–Pd–Pt–Ru†

Jan Lukas Bürgel, [a] Rico Zehl, [a] Felix Thelen, [a] Ridha Zerdoumi, [ab] Olga A. Krysiak, [b] Benedikt Kohnen, [a] Ellen Suhr, [a] Wolfgang Schuhmann [b] and Alfred Ludwig *[a]

Received 19th May 2025, Accepted 5th June 2025
DOI: 10.1039/d5fd00082c

Electrocatalysis is critical for mitigating climate change by providing green energy solutions, *e.g.* for hydrogen production by electrolysis of water implying high catalytic activity not only for hydrogen evolution but also for oxygen evolution as the counter reaction. Moreover, reactions such as oxygen reduction and nitrate reduction are of high importance in fuel cells or for environmental remediation. This study focuses on the exploration of electrocatalysts in the enormous composition spaces encountered in multinary materials like high-entropy alloys in the form of compositionally complex solid solutions. These provide paradigm-changing design principles for new electrocatalysts based on their tuneable surface atom arrangements resulting from their multinary composition. However, to master the combinatorial explosion problem of polyelemental catalysts, efficient exploration approaches need to be adapted. For this purpose, we present a comprehensive strategy to compare the electrocatalytic activity for different reactions in alkaline media, namely the oxygen evolution reaction (OER), oxygen reduction reaction (ORR), hydrogen evolution reaction (HER) and nitrate reduction reaction (NO_xRR) over large compositional spaces in three multinary systems: Cu–Pd–Pt–Ru, Ir–Pd–Pt–Ru and Ni–Pd–Pt–Ru. To generate the necessary large and multidimensional experimental dataset, thin-film materials libraries were synthesised and analysed using high-throughput characterisation methods. This allows for a comparative overview over correlations between composition and electrocatalytic activity, considering also relevant information on crystal structure and surface morphology. Similarities and differences, trends, maxima and minima in electrocatalytic

[a]*Chair for Materials Discovery and Interfaces, Institute for Materials, Faculty of Mechanical Engineering, Ruhr University Bochum, Universitätsstraße 150, 44801 Bochum, Germany. E-mail: alfred.ludwig@rub.de*
[b]*Analytical Chemistry – Center for Electrochemical Sciences (CES), Faculty of Chemistry and Biochemistry, Ruhr University Bochum, Universitätsstraße 150, 44801 Bochum, Germany*
† Electronic supplementary information (ESI) available. See DOI: https://doi.org/10.1039/d5fd00082c

activity are revealed and discussed. Main findings include that for the OER $Ir_{23}Pd_3Pt_8Ru_{66}$ exhibits the highest activity, exceeding any alloy of the other two systems by 51% (Ni–Pd–Pt–Ru) and 74% (Cu–Pd–Pt–Ru). For HER, $Ir_{36}Pd_4Pt_{48}Ru_{12}$ surpasses any of its elemental constituents by 26% and maxima in other systems by 5% (Ni–Pd–Pt–Ru) and 23% (Cu–Pd–Pt–Ru). For the NO_xRR, only a marginal increase of 4% was found between the most active measured alloy and the elemental constituent Cu. By comparing activity across systems, we demonstrate the tunability of electrochemical activity on compositionally complex solid solutions, achievable through variations in composition both within and across different material systems for four different reactions.

Introduction

Electrocatalysis is emerging as a pivotal field in addressing climate change, offering alternative energy sources and solutions for environmental remediation.[1,2] Central to this are key electrochemical reactions such as the HER, OER, ORR and NO_xRR.[3,4] For these and other electrochemical reactions new sustainable catalysts are urgently needed. Therefore, it is essential to discover optimal catalysts in an accelerated way.

High-entropy alloys (HEAs), specifically those forming solid solutions (compositionally complex solid solutions – CCSS), are promising for future electrocatalysts, due to underlying inherent characteristics.[5–8] The random distribution of several different atoms on the solid solution surface results in an immense number of possible surface atom arrangements (configurations of polyelemental sites). Since the electrochemical properties of an active site are influenced not only by one specific atom but also by its nearest neighbours, different arrangements of surface atoms display diverse characteristics. The result is a broad range of binding energies across the CCSS surface. Some sites offer optimal energetic environments for a reactant while others bind them either too strongly or too weakly. This presents both a challenge and an opportunity: on the one hand, it enables the possibility of tuning the surface composition to maximise the density of highly active catalytic sites for specific reactants or intermediates, optimising the catalyst for a specific reaction or even reaction pathway. On the other hand, it complicates the design of catalysts by increasing the compositional complexity, thus leading to a combinatorial explosion of possible multi-element systems and their respective compositional landscapes.

To overcome this challenge, we use a high-throughput approach based on synthesising and screening thin-film materials libraries, exhibiting well-controlled compositional gradients of all constituents.[9] Three quaternary composition spaces were selected: X–Pd–Pt–Ru with X = Cu, Ir, Ni. The pure elements Pd,[10,11] Pt[12] and Ru,[13] exhibiting high activity in many electrochemical applications, were combined to form the ternary base of the investigated quaternary alloys. Ir, which is also known to be highly active, was included to potentially yield an optimised, albeit costly, catalyst.[14,15] The influence of more affordable and sustainable constituents was investigated by adding Ni[16,17] or Cu[18] to the base of Pd–Pt–Ru. Using the high-throughput approach, the composition spaces were systematically explored, providing insights into the adjustability of the electrochemical activity achievable through compositional tuning within a given system and the changes encountered by exchanging constituents. This

was investigated for four different electrochemical reactions in alkaline media: OER, ORR, HER, and NO_xRR. Collectively, these reactions represent both reduction and oxidation reactions, different levels of complexity with respect to number of reaction intermediates and steps and involve reactants and products in the gas and liquid phase.

Experimental methods

The search spaces X–Pd–Pt–Ru with X = Cu, Ir and Ni were screened for their chemical compositions realised in the libraries and electrochemical activity as well as surface morphology and crystal structure, to assure comparability. Materials libraries (MLs) were synthesised by magnetron-co-sputtering using a sputter system ("Polaris 5-9000", AJA) with four cathodes ("InternationalModel ST15-P", AJA). The alignment of the cathodes to form the compositional gradients is outlined in Fig. 1a.

Three DC-power supplies were used: two model "DCXS-1500-4" (AJA) and one model "DCXS-750-4" (AJA). Furthermore, one RF-source was used ("0313 GTC",

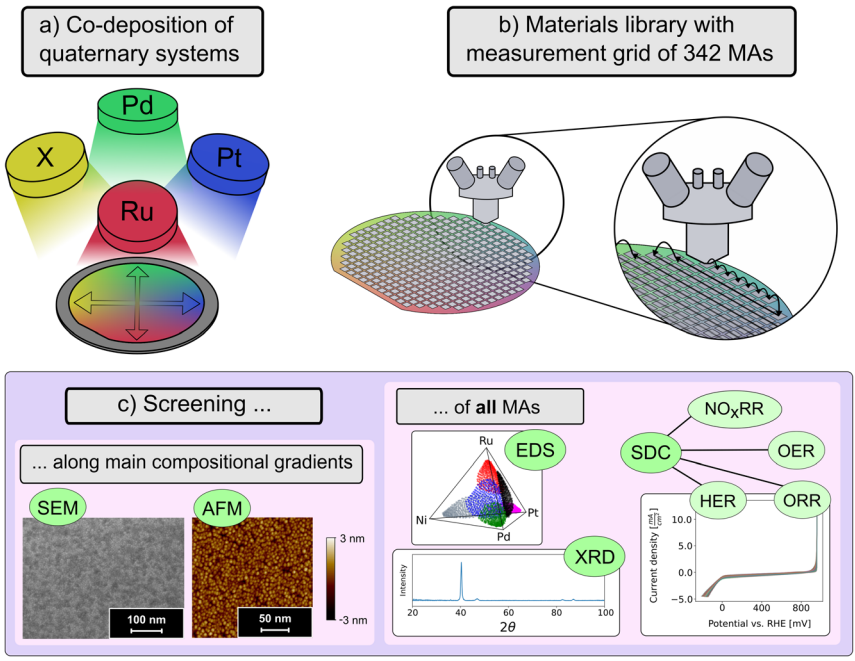

Fig. 1 Overview of the used high-throughput methods. (a) Combinatorial sputter synthesis of thin-film materials libraries which comprise (b) 342 measurement areas (MAs). (c) All MAs are investigated with high-throughput characterisation (screening) methods: energy dispersive X-ray spectroscopy (EDS) for compositional data, X-ray diffraction (XRD) for phase analysis, and linear sweep voltammetry using a scanning droplet cell (SDC) for electrochemical data of the hydrogen evolution reaction (HER), oxygen evolution reaction (OER), oxygen reduction reaction (ORR) and nitrate reduction reaction (NO_xRR). Selected MAs along the compositional gradients were analysed for surface morphology using scanning electron microscopy (SEM) and atomic force microscopy (AFM), representative results are shown in (c).

AJA) coupled with an "AIT-600 RF Autotuner" (AJA). The depositions were done in Ar-atmosphere at a pressure of 0.5 Pa at room temperature, *i.e.* without intentional heating. Elemental targets with 3.81 cm diameter were used: Ir (99.95% EVOCHEM Advanced Materials), Pd (99.9% Sindlhauser Materials), Pt (99.99% ESG Edelmetallservice), Ru (99.99% EVOCHEM Advanced Materials), Ni (99.99% EVOCHEM Advanced Materials), Cu (99.99% EVOCHEM Advanced Materials). The thin films were deposited on 100 mm diameter sapphire substrates (c-cut, SITUS-Technicals). To limit the use of the expensive materials, a film thickness of 100 nm was targeted. Deposition parameters are listed in the ESI.† First, one ternary ML was synthesised in the base system Pd–Pt–Ru. Following the method of Thelen *et al.*,[19] five different MLs were synthesised in each of the three quaternary composition spaces. One ML was fabricated around the equiatomic composition, whereas four additional MLs were synthesised in each corner of the composition spaces (where the composition of one of the constituent elements is highest, *i.e.* on the ML substrate level close to the respective deposition source).

After synthesis, 342 square-shaped measurement areas (MAs) with a size of 4.5 mm × 4.5 mm were defined on each ML (Fig. 1b) and investigated for their chemical composition with energy dispersive X-ray spectroscopy (EDS), their phase constitution (crystal structures, single- or multiphase) with X-ray diffraction (XRD) and their electrochemical activity with linear sweep voltammetry (LSV) in an automatic scanning droplet cell (SDC). In total 16 MLs were synthesised comprising 5472 MAs. To put the electrochemical results of the alloy systems into context, additional thin films of the six elemental constituents were sputtered and measured for their activity.

For the analysis of the chemical composition, a scanning electron microscope (SEM) ("JSM-5800 LV", JEOL) with an EDS-Detector ("INCA X-act", Oxford Instruments) and a tungsten filament was used. Each MA was investigated with an acceleration voltage of 20 kV at a magnification of 600×. An acquisition time of 60 s per MA was chosen, the working distance was set to 10 mm and a deadtime of around 30% was maintained throughout the measurement. Before the measurements on each ML started, a calibration on a Co standard was performed. The measured spectra were quantified using the "INCA" software (Oxford Instruments). Afterwards the quantified compositions were normalized to calculate the composition of the thin films, excluding the signal measured from the sapphire substrate.

XRD-measurements were carried out with a diffractometer ("D8 Discover", Bruker), which utilizes a Cu X-ray source "Incoatec IμS High-Brilliance Microfocus" ($\lambda = 0.15418$ nm) and a two-dimensional detector ("Vantec-500"). Using this detector, diffractograms were recorded at the three positions of $2\theta = 40°$, 60° and 80°. With the detector measuring in a 40° range, diffractograms containing information on the angles from $2\theta = 20°$ to 100° were obtained. For each MA, the three recorded 2D-diffractograms were stitched together using the "DIFFRAC.EVA" software (Bruker) and converted to a 1D-diffractogram. The software was further used to subtract the background of the diffractograms (parameters: threshold = 0.5, curvature = 0.3).

Using a SDC, high-throughput electrochemical measurements for the alkaline HER, ORR, OER, and NO_xRR were conducted on each of the 342 MAs on the ML. The SDC uses a 3-electrode setup, containing a Pt-wire counter electrode and a Ag|AgCl|3 M KCl reference electrode. Both electrodes were placed inside the

SDC-tip made of polytetrafluorethylene (PTFE) which was automatically filled with electrolyte prior to each measurement. For the alkaline HER, ORR and OER, 0.05 M KOH was used as electrolyte, while 0.05 M KOH + 0.05 M KNO_3 was used for NO_xRR. During each measurement, the SDC-tip was lowered towards a MA and pressed onto the thin film with a predefined force, forming an electrochemical cell with the thin film serving as the working electrode. The circular opening of the tip ($d = 1$ mm) defined the area of the working electrode. Upon pressing the tip onto the sample's surface, a sequence of electrochemical measurements was automatically triggered. The activities were measured by linear sweep voltammetry at a scan rate of 10 mV s^{-1}. HER and ORR were measured in a single sweep starting at 1000 mV *vs.* reversible hydrogen electrode (RHE), the OER was measured from 1000 mV *vs.* RHE to 1850 mV *vs.* RHE and the NO_xRR was measured starting from 300 mV *vs.* RHE. The potentials were converted to the RHE using eqn (1) and the current was normalized by the geometric surface area of the working electrode.

$$U_{RHE} = U_{(Ag|AgCl\|3\ M\ KCl)} + 210\ mV + (59\ mV \times pH) \quad (1)$$

To rule out an influence on the activity trends caused by deviations of the active surface area, the nanocrystalline surface morphology (Fig. 1c) was investigated. Surface characterisation relied on SEM-imaging, providing qualitative views of the morphology. This was further supported by atomic force microscopy (AFM) to quantify surface roughness. Since both methods are time-intensive, these measurements were only performed on selected MAs per ML, along the main compositional gradients (Fig. 1a). SEM-images were created using a secondary electron detector in a SEM ("JSM-7200F", JEOL). The images were taken at an acceleration voltage of 20 kV and at a magnification of 100 000×. For the roughness measurements, an AFM ("Fast Scan", Bruker) was used with a "ScanAsyst-Air" tip in the "PeakForce Tapping" mode. The software "NanoScope Analysis 1.8" (Bruker) was used to process the data and calculate the roughness of the thin films.

Results and discussion

Fig. 2 shows the compositions of the ML sputtered in the ternary base system Pd–Pt–Ru on the library level (a) with pie charts for the 342 MAs, in the form of a ternary diagram (b), and in the three quaternary spaces (c). Using the high-throughput approach, the MLs comprised more than 20% of all possible quaternary compositions (22.59% for Ni–Pd–Pt–Ru, 21.96% for Ir–Pd–Pt–Ru and 23.32% for Cu–Pd–Pt–Ru). Coverages were calculated by the method outlined by Thelen *et al.*[19] The MLs in the corners of the quaternary composition spaces reached up to a maximum of 80 at% to 95 at% of the single element constituents.

Assuring comparability: investigation of phase constitution and surface morphology

For a comparative study over large compositional ranges, it is important that the materials being compared are indeed comparable. Therefore, we need to know their phase constitution and surface morphology. The latter is relevant as different surface morphologies (*e.g.* different roughness levels) could lead to

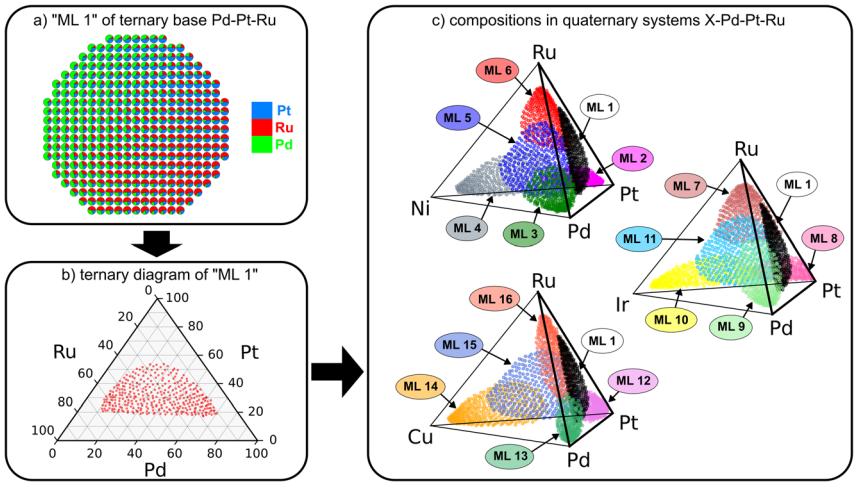

Fig. 2 Visualisation of the chemical compositions of the 5472 MAs from one ternary and three quaternary systems. In the ternary system Pd–Pt–Ru the composition of each MA is shown (a) as pie charts on the wafer level, and (b) in a ternary diagram. The compositions of all MAs in the three quaternary systems (c) from 16 MLs are shown as colour-coded point clouds in quaternary pyramid composition diagrams.

higher observed electrochemical current densities if normalisation is undertaken only with respect to the geometric area. However, if the surface morphologies across all MAs are similar, it is safe to interpret the observed activity trends to be caused by compositional changes. Furthermore, the crystal structure (fcc and/or hcp) could have an influence on activity. Two-phase regions could demonstrate complex behaviour, which could prove to be of interest but remains beyond the scope of a primary screening. However, trends observed for regions of the same phase constitution can be safely correlated with composition. The main interest in this comparative study is in single-phase solid solutions. Results of the XRD screening are shown in Fig. 3. The diffractograms of Pd-, Ni-, Cu-, Pt-, and Ir-rich compositions show a high-intensity reflection which shifts its position from $2\theta = 40°$ to 44° in dependence on composition. Other reflections around $2\theta = 47°$, 68°, 83°, and 88° exhibit a much lower intensity, but also display a composition-dependent 2θ-shift. This composition-dependent shift can be explained by Vegard's law, which states that in solid solutions the lattice parameters change linearly in correlation to the chemical composition.[20]

To verify the linearity of the observed pattern shift, a linear regression model was fitted to the 4-dimensional composition space based on tracking of the highest intensity reflection (Fig. S2†), creating a 4D-best-fit line. The method[22] is described in the ESI.† The coefficient of determination R^2 serves as an indicator of how well the fitted linear model matches the tracked experimental results, with an R^2 of 1 being a perfect match. R^2 was calculated for each system leading to a result of 0.98 for Ni–Pd–Pt–Ru, 0.98 for Cu–Pd–Pt–Ru and 0.945 for Ir–Pd–Pt–Ru, suggesting only a minor deviation of the experimental data from the linear fit. Even for the different hcp patterns in Ru-rich compositions, the accuracy of the model was still surprisingly high. By excluding Ru-rich (hcp) compositions, the accuracy

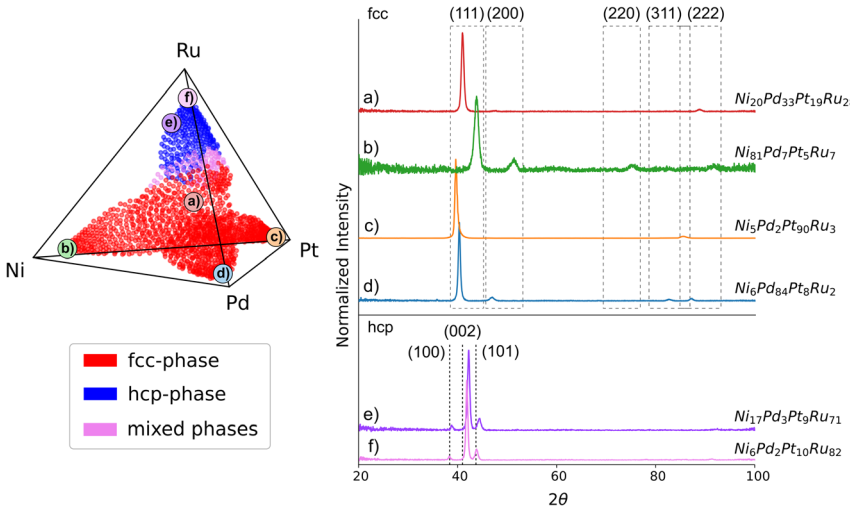

Fig. 3 Visualisation of the phase constitution on the example of the system Ni–Pd–Pt–Ru. Representative X-ray diffractograms are shown. The patterns match an fcc-structure in the Ni-, Pd-, Pt-rich and near-equiatomic region. Patterns in the Ru-rich region were identified as an hcp-structure and compared with [Pearson's Crystal Data 1244352].[21]

of the fit was only marginally increased to an R^2 of 0.99 for Ni–Pd–Pt–Ru, 0.99 for Cu–Pd–Pt–Ru and 0.95 for Ir–Pd–Pt–Ru. This, along with diffractograms showing only the pattern of one phase, indicates the presence of a single-phase solid solution in the Cu-, Ni-, Ir-, Pd- and Pt-rich as well as the near equiatomic compositional regions of the MLs.

By comparing the measured diffractograms with literature, it was inferred that an fcc-structure is present over most (*e.g.* 80% of the investigated MAs in the Ni–Pd–Pt–Ru system) of the investigated compositions. The reflection with the relatively high intensity around $2\theta = 42°$ was identified as a (111)-reflection, while the reflections around $2\theta = 47°$, 68°, 83° and 88° were identified as (200), (220), (311) and (222). Given that most pure constituents (Cu, Ir, Ni, Pd, Pt) of the multinary systems crystallise in an fcc-structure, the formation of an fcc-structure was expected. Pure Ru, however, exhibits an hcp-structure, leading to a change of pattern in the diffractograms of Ru-rich compositions (in the Ni–Pd–Pt–Ru system for Ru-contents higher than 55 at%), where reflections at $2\theta = 38°$, 41°, 44° were identified as (100), (002) and (101) of an hcp-phase.

The tracking of the high-intensity reflection over the composition spaces (Fig. S2†) revealed that the shift of the reflection was continuous, with no obvious discontinuities even in the Ru-rich compositional area. This continuity suggests that an overlap in reflection positions is present and thus indicates the presence of multiple phases, but all being present as solid solutions. It is likely that in the Ru-richest compositions, a single hcp-phase is present. Both the hcp single-phase and the fcc single-phase in the rest of the composition space should be separated by a two-phase region. However, preferential growth of the thin film led to a situation where there is only one reflection visible in the diffractograms. Other reflections, which would be used to identify a two-phase region or the lack

thereof, have a much lower intensity, disappearing in the transition between the single-phase regions. Consequently, a well-defined boundary between the regions cannot be identified. Fig. 3 illustrates the regions where the fcc- and hcp-phases as well as mixed phases are estimated to be present in the Ni–Pd–Pt–Ru system.

All thin films showed small grains in the range of 10 to 20 nm with a roughness on the nanoscale. Fig. 1c shows the surface morphology of the middle of ML 11 (near-equiatomic ML in the Ir–Pd–Pt–Ru system), representatively. Further SEM images along the compositional gradients can be found in the ESI.† The small grain size resulted in a high coverage of grain boundaries on the surface, which can lead to an increase in activity.[23] However, based on the SEM images no major deviations in grain size or surface morphology were observed along the compositional gradients.

Minor changes in the surface roughness in dependence on the chemical composition were detected with AFM. Ir-, Pt- and Ru-rich compositions showed a smaller degree of roughness than compositions rich in Pd, Ni and Cu (Ir < Pt ≈ Ru < Pd ≈ Cu ≈ Ni). A higher roughness should yield a higher active surface area and thus a higher activity. As such a material's intrinsic electrochemical activity in the Ir-, Ru- and Pt-rich regions should be higher than the ones that were measured, whereas activities in Pd-, Cu-, and Ni-rich compositions should be relatively lower.

Assessing the tunability of electrocatalytic activity in CCSS

After the determination of the phase constitution, and associated with it, the verification of the presence of solid solutions, the electrochemical activity was screened by linear sweep voltammetry (LSV) using a SDC setup. For each reaction, the current densities were compared at a specific potential (HER: −100 mV *vs.* RHE, OER: 1700 mV *vs.* RHE, ORR: 800 mV *vs.* RHE, NO_xRR: 50 mV *vs.* RHE). These specific potential values were chosen to analyse the LSVs in regions of linear change of current density, decreasing the complexity of the LSVs down to a one-dimensional value and giving simplified insights into the activity. An overview over the trends of the electrochemical activity for the OER, ORR, HER, and NO_xRR in correlation with the chemical composition is given in Fig. 4. The activities are displayed in the three different quaternary composition spaces in the form of a colourmap where red indicates the highest and blue the lowest activity for each reaction. The maxima found in each quaternary system as well as the base ternary system for each reaction are further shown in Table S3 in the ESI.†

The global OER activity maximum was identified in the system Ir–Pd–Pt–Ru (2.68 mA cm^{-2} at 1700 mV *vs.* RHE) and was achieved with the composition $Ir_{23}Pd_3Pt_8Ru_{66}$, surpassing the maximum observed in the Cu–Pd–Pt–Ru system by 67% (Fig. 5). A trend indicating an activity increase towards the binary system Ir–Ru was evident. This peak activity in the Ir–Ru-rich side of the composition space aligns well with the known efficacy of Ru–Ir-oxides,[24] one of the most active materials for the OER. Under reaction conditions, the initially metallic thin film is expected to form a multinary surface oxide. In the systems Ni–Pd–Pt–Ru and Cu–Pd–Pt–Ru, activity increased towards Ru-rich compositions. Both Pd- and Pt-rich compositions in the quaternary spaces showed decreased activity, even compared to the less costly Ni- and Cu-rich compositions.

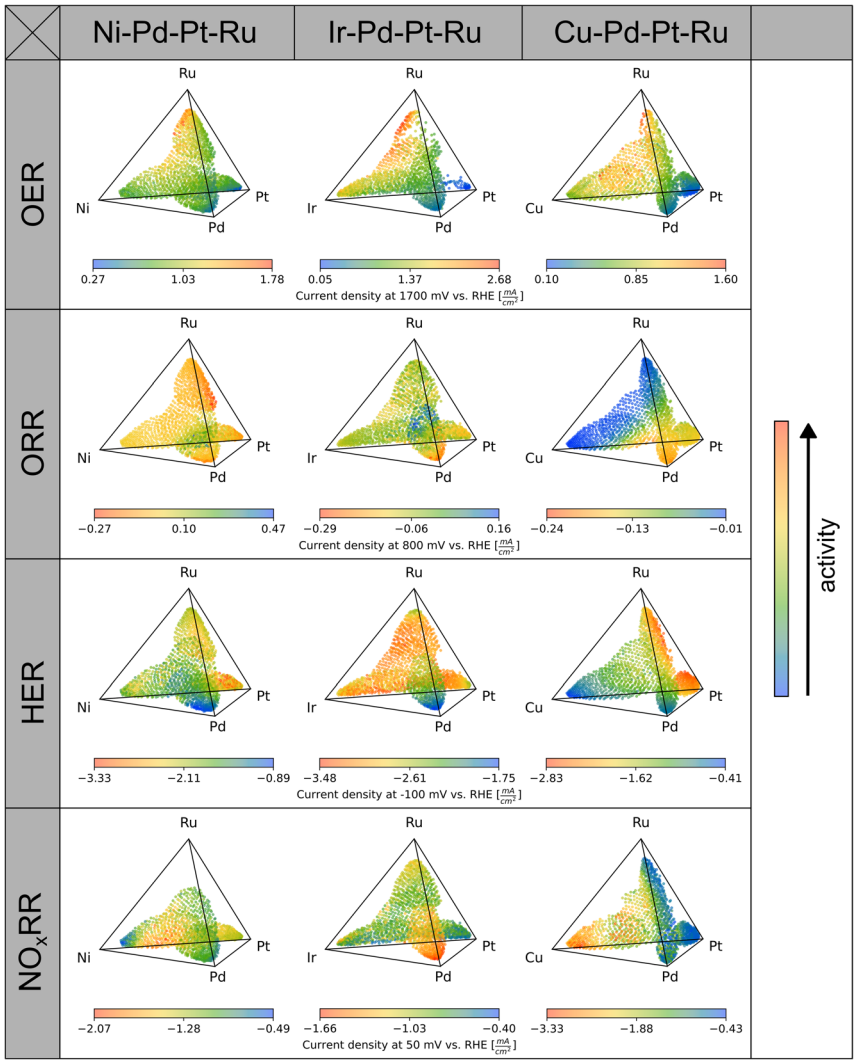

Fig. 4 Overview over the results of all electrochemical measurements in the three investigated quaternary systems. Current densities (colour coded: red – high activity, blue – low activity, within the respective system) were compared at specific potentials as a measure of activity. Outlier LSVs were excluded manually.

These findings were further evidenced by the electrochemical measurements of the constituents in the form of elemental thin film samples. Pure Ru exhibited seemingly the highest activity, surpassing any of the quaternary or ternary compositions measured by at least 250%. However, the LSV of Ru (Fig. S6†) indicated significant dissolution, suggesting that the apparent performance was partly due to instability of this material. Therefore, pure Ru was excluded from further comparative considerations for OER in this study. Lower activities were observed for the other elemental samples, with Pt, Cu and Pd exhibiting the lowest OER activity, being surpassed by most quaternary compositions. Notably,

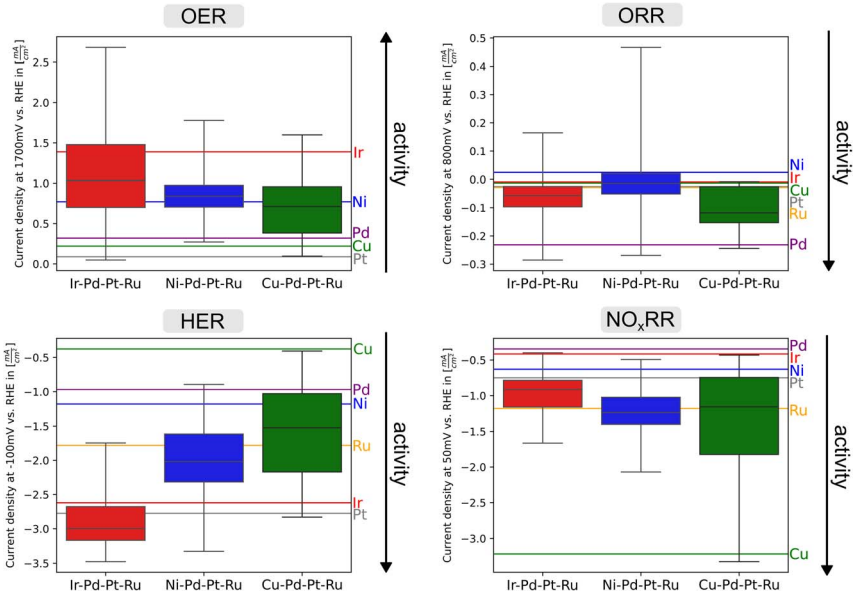

Fig. 5 Comparison of current densities measured for the four reactions at relevant potentials as an indication of activity in the three material systems in the form of boxplots. Boxes extend to the quartiles of the respective dataset, while whiskers indicate the whole distribution. For the OER, higher anodic current densities suggest higher activity, whereas higher cathodic current densities indicate higher activity for the ORR, HER, and NO_xRR. The material systems are further compared with the activities of single element reference samples, indicated by the horizontal lines in each diagram. For the OER, Ru was excluded, due to its limited stability under reaction conditions.

compositions showing an optimum in OER activity corresponded to an hcp-structure, as they had a high Ru-content. However, it remains unclear whether the observed peak activity can be attributed to intrinsic properties of Ru or to the presence of the hcp-structure, or the inclusion of Ru in a quaternary solid solution which could also help to stabilize it. A distinction between these factors was not made in this study but is an interesting topic for future research.

For the ORR, the observed trends indicated that a high Pd content positively impacts activity. The optimum was found in the Ir–Pd–Pt–Ru system at a composition of $Ir_8Pd_{82}Pt_6Ru_4$ at -0.29 mA cm^{-2}. Additionally, a high Pt content enhanced the ORR activity, although to a lesser extent than Pd. Regions rich in Cu, Ni, Ir, and Ru exhibited a decreasing trend in activity. However, the range between current densities of different compositions was smaller compared to the other reactions as evidenced by the optima in the systems Ni–Pd–Pt–Ru (-0.27 mA cm^{-2}) and the system Cu–Pd–Pt–Ru (-0.24 mA cm^{-2}). This limited range in measured current densities was partly caused by the measurement setup; the amount of oxygen which can be reduced is constrained to the volume of the electrolyte in the SDC-tip, resulting in a sluggish mass-transfer dominated ORR response. Pure Pd exhibited the highest activity among all measured constituent elements, which supports the measured activity trends. Positive current densities were observed at chosen reference potentials, indicating an oxidation current instead of the expected oxygen reduction current. Notably, these positive currents

were only observed in the Ir–Pd–Pt–Ru- and the Ni–Pd–Pt–Ru systems, not the Cu–Pd–Pt–Ru system.

In all three investigated systems, trends showing an increase in HER activity were observed towards the Pt-rich side and, to a lesser extent, to the Ru-rich side indicating maxima near or within the binary system Pt–Ru. The exception to this was observed in the system Ir–Pd–Pt–Ru where the global maximum of HER activity was found to be at a composition of $Ir_{36}Pd_4Pt_{48}Ru_{12}$, achieving −3.48 mA cm^{-2} at −100 mV *vs.* RHE. Furthermore, activity was high for Pt-, Ir- and Ru-rich compositions as evidenced by the fourth highest value of current density: −3.46 mA cm^{-2} found at $Ir_{26}Pd_8Pt_{17}Ru_{49}$; a significantly different composition, with lower Pt and higher Ru content, that yielded, however, almost the same current density as the maximum. A decreasing activity trend was visible both in compositions with highest Pt- and Ru-content (Fig. 6).

This indicates an activity maximum in the quaternary space, or more likely, within the ternary space Ir–Pt–Ru as higher Pd-content decreased HER activity in all investigated systems. The decrease in activity with an increase in Ru-content could also be influenced by the crystal structure. Cu decreased HER activity, as higher current density values were found in the ternary base system Pd–Pt–Ru than in any quaternary composition containing Cu. Conversely, Ni showed a more positive influence on HER activity, the optimum in the Ni–Pd–Pt–Ru system surpassing the maximum activity in the Cu–Pd–Pt–Ru as well as the ternary Pd–Pt–Ru system by 18%. This indicates that small amounts of Ni may have a positive impact on the HER activity. All quaternary systems contained compositions which surpassed all single element reference samples in activity. Of those reference samples Pt and Ir exhibited the highest HER activity. Interestingly, even the Cu–Pd–Pt–Ru system contained compositions which exhibited higher activity than the single element references, despite the presence of Cu, which showed a detrimental effect on the HER activity in the investigated systems. However, Cu–Pd–

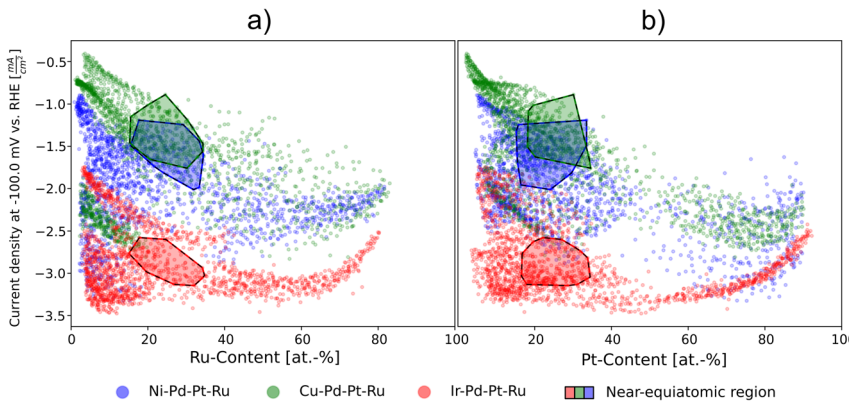

Fig. 6 Comparative HER activity plot from which correlations between the Ru-content (a) and the Pt-content (b) with the HER activity (indicated by the current density at −100 mV *vs.* RHE) can be inferred. The colour-coded markers show all compositions of the HER dataset. The near-equiatomic compositions (all constituents between 15 and 35 at%) of each system are framed. In the Pt-richest compositions a decrease in activity is observed in the Ir–Pd–Pt–Ru system (red). The Ru-richest compositions show a decreasing activity trend in all systems.

Pt–Ru only surpassed pure Pt marginally. The activity maximum of the Ni–Pd–Pt–Ru space exceeded pure Pt by 20%, while the Ir–Pd–Pt–Ru system surpassed it by 26%. The measured activity trends for the OER and HER indicated maximal activities in Ir-, Ru- and Pt-rich compositions, suggesting that these trends would remain unchanged, if potential deviations in surface roughness were included.

Fig. 6 highlights near-equiatomic compositions, defined here as all constituents ranging between 15 and 35 at%. These composition regions are commonly investigated in the research of HEAs due to the maximised mixing entropy in this region. However, in this study, none of the near-equiatomic compositions corresponded to the observed maxima in catalytic activity. This underlines the importance of extending the investigation beyond the near-equiatomic region to find optimal catalysts for different reactions.

The global maximum of activity for the NO_xRR was observed in the Cu–Pd–Pt–Ru system, specifically in Cu-rich compositions. This suggests that Cu exhibits a more positive impact on activity than any of the precious metals investigated (Pt, Pd, Ru, Ir). This finding is corroborated by Wan *et al.*[25] who predicted Cu to exhibit high activity for the NO_xRR, adding that Cu could also yield a higher selectivity for the reaction. Comparing the alloys to the best performing single element reference Cu, only a small increase in activity of 4% was detected. The NO_xRR results of the Ru-rich ML in the Ni–Pd–Pt–Ru system (ML 6) were excluded due to a faulty measurement. Without it, a maximum in activity was identified within the quaternary composition space centred around $Ni_{41}Pd_{37}Pt_8Ru_{14}$. Yet, this maximum ($-2.07$ mA cm^{-2}) was substantially lower than the one observed in the Cu–Pd–Pt–Ru system (-3.33 mA cm^{-2}). The Ir–Pd–Pt–Ru system exhibited an even lower maximal activity at -1.66 mA cm^{-2}. In contrast to the other reactions, different trends were observed across the three different quaternary systems: a maximum in the Pd-rich region in the Ir–Pd–Pt–Ru system, a maximum within the quaternary space in the Ni–Pd–Pt–Ru system and a maximum in the Cu-richest region in the Cu–Pd–Pt–Ru system. These differences may be caused by the complexity of the NO_xRR, which involves multiple intermediates that favour adsorption at different active sites. While activity trends for the NO_xRR indicated optima in Cu-rich compositions, which showed a rougher surface, the range of current densities in the composition space was quite large, making it unlikely that these trends would be significantly affected by changes in the roughness of the thin films.

The investigation of the OER, ORR, HER, and NO_xRR revealed that each reaction exhibits distinct trends in activity, strongly influenced by the chemical composition of the catalyst. It was expected that different reactants and intermediates require dissimilar adsorption energies and that such dissimilar adsorption energies could be reached by altering the composition of the catalyst material. This expectation was confirmed, as significant changes in activity were observed by altering just one of the constituents of a quaternary system. Different reactions responded differently to the same compositional changes, highlighting the complexity in catalyst design. Ru-rich compositions enhanced the OER, while Pd increased the ORR activity. Cu suppressed the HER but substantially improved the NO_xRR activity. Such a contrasting effect on competing reactions could also provide the possibility of drawing qualitative conclusions on the selectivity of catalysts or individual constituents.

Interestingly, the trend in the Ir–Pd–Pt–Ru system for NO_xRR looked almost inverted to the HER trend in this system. Identifying such trends within this large dataset becomes challenging for a human researcher, as the volume of data makes it difficult to efficiently analyse and correlate results. However, interactive visualisation tools, *e.g.* "parallel coordinates"[26] can help to visualise complex and large datasets. An interactive plot of parallel coordinates is supplied in the ESI.† In Fig. 7a, the compositions with the highest OER activity are highlighted and coloured (red indicates high, blue indicates low activity). Notably, compositions exhibiting high OER activity also show high HER activity. However, the reverse is not true, as illustrated in Fig. 7b, which shows that compositions that are most active for HER exhibit varying levels of OER activity.

One question was whether the observed trends could have been qualitatively predicted from the activities of single element samples. For the OER, Ru was seemingly the most active single element, although this may have been caused by Ru dissolution. The high activity was reflected in the alloy trends. However, the highest activity was found to be in the binary Ir–Ru. In the case of the HER, Pt, Ru, and Ir were the most active single element materials. Trends indicated a maximum to be present in a ternary alloy containing these constituents. However, the alloys outperformed their constituents indicating a synergistic effect. Another synergistic effect was observed for the NO_xRR in the Ni–Pd–Pt–Ru system. Some trends could have been inferred based on the single element reactions. This was particularly evident in cases where one element significantly outperformed all other constituents, such as Cu for the NO_xRR. Yet, the synergistic effects we aim to achieve with HEA catalysts could not have been predicted from single element activities alone.

Notably, a higher variability in activity could be detected within composition spaces than between them. For instance, in the Ni–Pd–Pt–Ru system, HER current

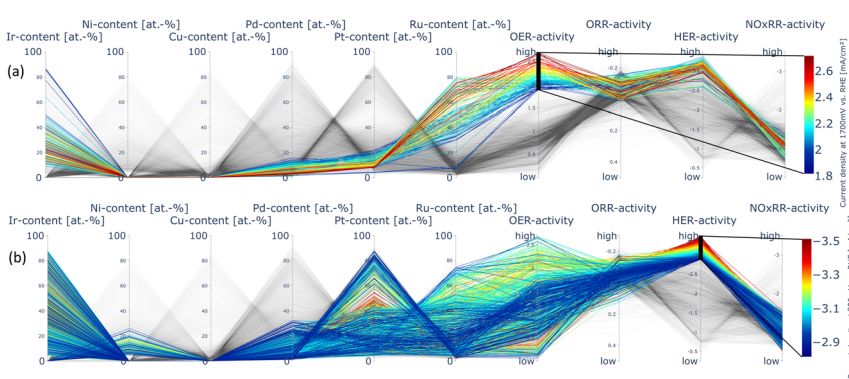

Fig. 7 Two examples of comparative analysis of the complete investigated dataset by parallel coordinate plots (interactive plot in the ESI†): each of the vertical axes represents one of the investigated parameters, such as constituent content or electrochemical activities. Each line represents one data point comprising composition and measured activities for the four reactions; (a) compositions exhibiting the highest OER activity are marked and colour coded. The plot shows that these compositions correlate also with high HER activity; (b) compositions showing the highest HER activity are marked and colour coded. The plot shows that these compositions do not correlate with high OER activity.

densities at −100 mV *vs.* RHE ranged from −1 to −3.33 mA cm^{-2}. The replacement of Ni with Ir led to only a marginal increase of the optimum to −3.48 mA cm^{-2}. By alloying Cu instead, a global minimum of activity was reached, indicated by a current density of −0.41 mA cm^{-2}. This activity overlap (Fig. 5) between the systems could be attributed to Pt and Ru, which dominate the catalytic response and compensate for less active constituents like Cu. This emphasises that thoroughly screening a given multi-element space is as important as it is to explore another one. In this study approximately 20% of each composition space was covered. In a previous work,[19] it was concluded that a coverage of 20% would be sufficient to identify trends in activity. We identified such trends in multiple composition spaces and for various reactions, affirming prior findings. The fact that many activity maxima were observed either within compositions rich in one constituent or less complex systems, *i.e.* ternary, binary or single elements highlights the importance to not only measure the equiatomic composition but also corners of the composition space.

The measured trends were mostly continuous across the composition spaces, supporting the assumption of a solid solution being present, where gradual changes in surface composition led to a corresponding shift in reactant adsorption energy and following this, the electrochemical activity. However, the surface composition itself was not directly measured. Instead, the electrochemical activity was correlated to the volume compositions. Segregation effects caused by the synthesis, the storage of the samples (in air) or the measurements could have led to deviations between surface and volume compositions.

Ensuring data quality is an important aspect of high-throughput experimentation. Despite challenges such as possible surface segregation, oxidation or uncertainty about the phase constitution, the consistency of the observed trends for the OER, HER and NO_xRR suggests that the data was of sufficient quality to extract meaningful insights. The ORR data, however, was less consistent due to the limited oxygen dissolution in the electrolyte, suggesting the need for improved measurement setups for reactions involving gaseous reactants. However, qualitative trends were still discernible. The presented trends could be observed even before data processing, further emphasising the robustness of the results. This also suggests that the veracity of individual data points is less critical, if the overall trend is clear, which is enabled by the MLs.

Simplifying LSVs to a single data point (*e.g.* current density at a fixed reference potential) offers the means to compare such a large amount of LSVs, but it also means a substantial loss of information. Important features of the LSVs could be overlooked and as such misrepresent catalytic performance. For instance, the ORR and HER were measured in one sweep in this study, leading to a possible influence of the ORR on the HER datapoints. In our case the ORR current densities were limited, which led to the ORR contribution to the HER current being negligible. For less stable materials, such as Ru under OER conditions, the shape of the LSVs (Fig. S6†) revealed that the measured current was partially caused by material dissolution. In this case, relying solely on a single current density value would have misleadingly suggested Ru to be by far the best catalyst for alkaline OER. As such, more comprehensive methods to compare whole LSVs instead of selected current density values should be implemented in future high-throughput data-processing approaches.

Multi-objective optimisation of catalysts

Optimisation of catalysts involves balancing multiple objectives such as activity, stability, selectivity and cost. The Pareto front is a concept in multi-objective optimisation, representing a set of non-dominated solutions where no objective can be improved without worsening another. Fig. 8 visualises Pareto fronts of the investigated activities and the material cost of the catalysts.[27]

For the OER, pure Ni stands out due to its low cost with limited activity. Of the investigated alloys, materials of all three investigated quaternary systems are part of the Pareto front. Alloys of the Cu–Pd–Pt–Ru system are only slightly more active than pure Ni but come with a substantial increase in cost due to the noble metal constituents. The Ni–Pd–Pt–Ru system exhibits slightly higher activity, while also increasing the cost marginally. Transitioning from Ni–Pd–Pt–Ru to Ir–Pd–Pt–Ru resulted in a significant increase in cost of up to 269%, while yielding only a moderate improvement in activity of 51%. For the ORR, the Pareto front is dominated by quaternary alloys of the Ni–Pd–Pt–Ru system. Alloys containing Ir show only a slight increase in activity compared to the Ni–Pd–Pt–Ru system, but this comes with a significantly higher price. In the case of the HER, pure Ni emerges as a cost-effective catalyst. Additionally, mostly alloys of the Ni–Pd–Pt–Ru system are part of the Pareto front, combining the comparatively inexpensive Ni with the more active noble metals, specifically Pt. Only a marginal activity increase of up to 5% is observed in compositions containing Ir, compared to

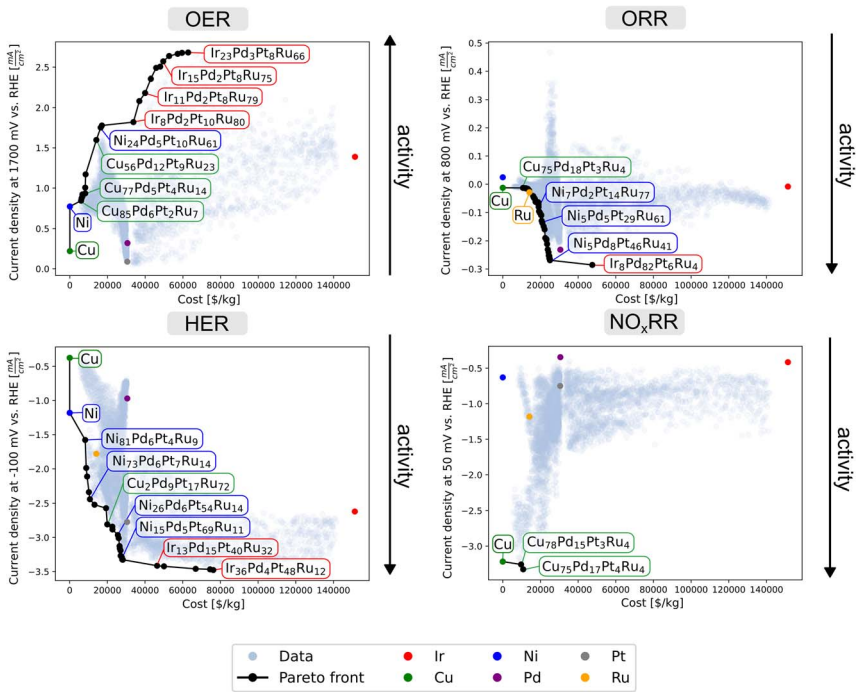

Fig. 8 Pareto fronts for the electrochemical activity of the four reactions *vs.* the cost of the catalysts.[27] Single element samples are marked in different colours. Representative quaternary compositions along the Pareto front are indicated.

those containing Ni, while the cost increases significantly. For NO_xRR, only three compositions make up the Pareto front, pure Cu being one of them. The alloys of the Cu–Pd–Pt–Ru system only offer a small increase in activity compared to Cu, while being considerably more costly. Thus, Cu appears to be optimal within the group of investigated catalyst materials regarding a cost *vs.* NO_xRR activity analysis. Both pure Cu and Ni are frequently part of the constructed Pareto fronts, due to their much lower prices compared to noble-metal constituents. This extends to the investigated alloys, since alloys containing Cu and Ni are much less expensive than those containing Ir. While Ir did increase the electrochemical activity for the HER and ORR, these increases were only marginal and came with a substantial increase in price. Therefore, the inclusion of Ir based on activity and cost alone does not appear to be justifiable.

In the future, the exploration of multi-element material systems will further extend the complexity of datasets. In this context, machine learning models provide a rising potential to help in analysing and interpreting these ever-growing datasets, enabling the identification of activity maxima as well as broader trends. Including additional optimisation parameters, such as cost, stability or selectivity into such models will help in enabling the discovery of optimised catalyst materials. To effectively identify trends, it is important to achieve a broad coverage of material systems. An increasing chemical complexity of HEAs results in an exponential expansion of the composition spaces, making comprehensive exploration more challenging. This highlights the need to refine high-throughput methodology either with more complex library design, like micro-libraries,[28] with systematic approaches such as backward elimination,[29] or with the inclusion of simulations into the high-throughput workflow.[30,31]

Conclusion

The three quaternary systems Ni–Pd–Pt–Ru, Cu–Pd–Pt–Ru and Ir–Pd–Pt–Ru were screened for their activity for four different electrochemical reactions in alkaline media: the OER, the ORR, the HER and the NO_xRR. By using a high-throughput approach, large portions of the composition spaces were efficiently explored with a relatively small number of samples. This methodology enabled the identification of activity maxima, many of which were located outside the commonly studied near-equiatomic composition region, underscoring the importance of broad compositional coverage when studying CCSS-catalysts. By analysing the multidimensional dataset, distinct activity trends were discovered and correlated to changes in chemical composition. Specifically, $Ir_{23}Pd_3Pt_8Ru_{66}$ exhibited the maximum activity for the OER, indicating activity maxima to be in the region close to binary system Ir–Ru. For the HER, alloys rich in Ru, Pt and Ir demonstrated the highest activity, with small amounts of Ni also contributing positively. The most active catalysts for the ORR were rich in Pd, with Pt playing also a positive, though less important role. Trends for the NO_xRR indicated Cu-rich compositions to have the highest activity, only marginally exceeding pure Cu by 4%, but increasing the material price substantially. Beyond activity, this study highlighted the need to include additional design criteria such as cost, stability or selectivity. For instance, while the Ir–Pd–Pt–Ru system exhibited high activity for the OER, ORR and HER, it came with a substantially higher material cost compared to the other two systems. In future works, the introduced approach could be extended to explore multiple

reactions occurring at overlapping potentials, offering insight into how compositional tuning favours one reaction over the other.

Data availability

Data for this article, including the electrochemical dataset, compositional dataset, the diffractograms and the interactive parallel coordinates plot, are available at Zenodo under **https://doi.org/10.5281/zenodo.15453660**. Further data supporting this article have been included in the ESI.†

Author contributions

J. L. Bürgel: conceptualization, sample fabrication, measurement, data curation, formal analysis, visualisation, writing – original draft; R. Zehl: conceptualization, sample fabrication, measurement, data curation, visualisation, formal analysis, software, writing – review & editing; F. Thelen: conceptualization, sample fabrication, measurement, data curation, visualisation, formal analysis, software, writing – review & editing; R. Zerdoumi: measurement, writing – review & editing; O. A. Krysiak: measurement; B. Kohnen: measurement; E. Suhr: measurement; W. Schuhmann: conceptualization, supervision, resources, writing – review & editing; A. Ludwig: conceptualization, supervision, funding acquisition, resources, project administration, writing – original draft.

Conflicts of interest

There are no conflicts to declare.

Acknowledgements

This work was partially supported from different projects. A. Ludwig, J. L. Bürgel and F. Thelen acknowledge funding from the European Union through the European Research Council (ERC) Synergy Grant project 101118768 (DEMI). Funded by the European Union, views and opinions expressed are however those of the author(s) only and do not necessarily reflect those of the European Union or European Research Council Executive Agency. Neither the European Union nor the granting authority can be held responsible for them. Funding by the Deutsche Forschungsgemeinschaft (DFG, German Research Foundation) CRC 1625, project number 506711657, subproject A02 is acknowledged by R. Zehl and A. Ludwig, as well as subproject C01 by W. Schuhmann. The authors acknowledge using ZGH infrastructure for measurements (Scanning Electron Microscope, X-Ray Diffractometer, Atomic Force Microscope).

References

1 S. Trasatti, *Int. J. Hydrogen Energy*, 1995, **20**, 835–844.
2 Q. Jiang, K. Jiang, Y. Ye, K. Xi and C. Xia, *Front. Chem.*, 2023, **11**, 1159716.
3 M. Duca and M. T. M. Koper, *Energy Environ. Sci.*, 2012, **5**, 9726.
4 V. Rosca, M. Duca, M. T. de Groot and M. T. M. Koper, *Chem. Rev.*, 2009, **109**, 2209–2244.

5 T. A. Batchelor, J. K. Pedersen, S. H. Winther, I. E. Castelli, K. W. Jacobsen and J. Rossmeisl, *Joule*, 2019, **3**, 834–845.
6 L. Han, S. Zhu, Z. Rao, C. Scheu, D. Ponge, A. Ludwig, H. Zhang, O. Gutfleisch, H. Hahn, Z. Li and D. Raabe, *Nat. Rev. Mater.*, 2024, **9**, 846–865.
7 T. Löffler, A. Ludwig, J. Rossmeisl and W. Schuhmann, *Angew. Chem., Int. Ed.*, 2021, **60**, 26894–26903.
8 T. Löffler, A. Savan, A. Garzón-Manjón, M. Meischein, C. Scheu, A. Ludwig and W. Schuhmann, *ACS Energy Lett.*, 2019, **4**, 1206–1214.
9 A. Ludwig, *npj Comput. Mater.*, 2019, **5**, 70.
10 H. Li and G. Li, *J. Mater. Chem. A*, 2023, **11**, 9383–9400.
11 M. Shao, *J. Power Sources*, 2011, **196**, 2433–2444.
12 G. Gao, G. Zhu, X. Chen, Z. Sun and A. Cabot, *ACS Nano*, 2023, **17**, 20804–20824.
13 C. Hu, J. Xu, Y. Tan and X. Huang, *Trends Chem.*, 2023, **5**, 225–239.
14 B. Huang and Y. Zhao, *EcoMat*, 2022, **4**, e12176.
15 C. Li and J.-B. Baek, *ACS Omega*, 2020, **5**, 31–40.
16 Z. Angeles-Olvera, A. Crespo-Yapur, O. Rodríguez, J. Cholula-Díaz, L. Martínez and M. Videa, *Energies*, 2022, **15**, 1609.
17 V. Vij, S. Sultan, A. M. Harzandi, A. Meena, J. N. Tiwari, W.-G. Lee, T. Yoon and K. S. Kim, *ACS Catal.*, 2017, **7**, 7196–7225.
18 Y. Wang, W. Zhou, R. Jia, Y. Yu and B. Zhang, *Angew. Chem., Int. Ed.*, 2020, **59**, 5350–5354.
19 F. Thelen, R. Zehl, R. Zerdoumi, J. L. Bürgel, L. Banko, W. Schuhmann and A. Ludwig, *Adv. Sci.*, 2025, e07302.
20 A. R. Denton and N. W. Ashcroft, *Phys. Rev. A: At., Mol., Opt. Phys.*, 1991, **43**, 3161–3164.
21 K. C. P. Villars, *Pearson's Crystal Data: Crystal Structure Database for Inorganic Compounds (On DVD)*, ASM International®, Materials Park, Ohio, USA, 2023/24.
22 F. Pedregosa, G. Varoquaux, A. Gramfort, V. Michel, B. Thirion, O. Grisel, M. Blondel, P. Prettenhofer, R. Weiss, V. Dubourg, J. Vanderplas, A. Passos, D. Cournapeau, M. Brucher, M. Perrot and É. Duchesnay, *J. Mach. Learn. Res.*, 2011, **12**, 2824–2830.
23 X. Geng, M. Vega-Paredes, Z. Wang, C. Ophus, P. Lu, Y. Ma, S. Zhang, C. Scheu, C. H. Liebscher and B. Gault, *Nat. Commun.*, 2024, **15**, 8534.
24 S. Cherevko, S. Geiger, O. Kasian, N. Kulyk, J.-P. Grote, A. Savan, B. R. Shrestha, S. Merzlikin, B. Breitbach, A. Ludwig and K. J. Mayrhofer, *Catal. Today*, 2016, **262**, 170–180.
25 H. Wan, A. Bagger and J. Rossmeisl, *Angew. Chem., Int. Ed.*, 2021, **60**, 21966–21972.
26 Plotly Technologies Inc., *Collaborative Data Science*, Plotly Technologies Inc., Montréal, QC, 2015.
27 Deutsche Rohstoffagentur, Bundesanstalt für Geowissenschaften und Rohstoffe, *Preismonitor*, Januar, 2025, available at: **https://www.deutsche-rohstoffagentur.de/DE/Themen/Min_rohstoffe/Produkte/Preisliste/pm_25_01.pdf;jsessionid=21F0EDB5484A2121C0CF037F80F7521C.internet942?__blob=publicationFile&v=2**, accessed 13 May 2025.

28 L. Banko, E. B. Tetteh, A. Kostka, T. H. Piotrowiak, O. A. Krysiak, U. Hagemann, C. Andronescu, W. Schuhmann and A. Ludwig, *Adv. Mater.*, 2023, **35**, e2207635.
29 V. Mints, J. K. Pedersen, G. K. H. Wiberg, J. Rossmeisl and M. Arenz, Backward Elimination: A Strategy for High-Entropy Alloy Catalyst Discovery, *ChemRxiv*, 2022, preprint, DOI: **10.26434/chemrxiv-2022-78s83**.
30 C. M. Clausen, O. A. Krysiak, L. Banko, J. K. Pedersen, W. Schuhmann, A. Ludwig and J. Rossmeisl, *Angew. Chem., Int. Ed.*, 2023, **62**, e202307187.
31 T. A. A. Batchelor, T. Löffler, B. Xiao, O. A. Krysiak, V. Strotkötter, J. K. Pedersen, C. M. Clausen, A. Savan, Y. Li, W. Schuhmann, J. Rossmeisl and A. Ludwig, *Angew. Chem., Int. Ed.*, 2021, **60**, 6932–6937.